NANO LETTERS

Letter

pubs.acs.org/NanoLett

Local Enhancement of Polarization at $PbTiO_3/BiFeO_3$ Interfaces Mediated by Charge Transfer

Ying Liu,[†] Yin-Lian Zhu,[*,†] Yun-Long Tang,[†] Yu-Jia Wang,[†] Yi-Xiao Jiang,[†] Yao-Bin Xu,[†] Bin Zhang,[‡] and Xiu-Liang Ma[*,†,§]

[†]Shenyang National Laboratory for Materials Science, Institute of Metal Research and [‡]Analysis and Testing Department, Institute of Metal Research, Chinese Academy of Sciences, Wenhua Road 72, 110016 Shenyang, China

[§]School of Materials Science and Engineering, Lanzhou University of Technology, Langongping Road 287, 730050 Lanzhou, China

S *Supporting Information*

ABSTRACT: Ferroelectrics hold promise for sensors, transducers, and telecommunications. With the demand of electronic devices scaling down, they take the form of nanoscale films. However, the polarizations in ultrathin ferroelectric films are usually reduced dramatically due to the depolarization field caused by incomplete charge screening at interfaces, hampering the integrations of ferroelectrics into electric devices. Here, we design and fabricate a ferroelectric/multiferroic $PbTiO_3/BiFeO_3$ system, which exhibits discontinuities in both chemical valence and ferroelectric polarization across the interface. Aberration-corrected scanning transmission electron microscopic study reveals an 8% elongation of out-of-plane lattice spacing associated with 104%, 107%, and 39% increments of δ_{Ti}, δ_{O1}, and δ_{O2} in the $PbTiO_3$ layer near the head-to-tail polarized interface, suggesting an over ~70% enhancement of polarization compared with that of bulk $PbTiO_3$. Besides that in $PbTiO_3$, polarization in the $BiFeO_3$ is also remarkably enhanced. Electron energy loss spectrum and X-ray photoelectron spectroscopy investigations demonstrate the oxygen vacancy accumulation as well as the transfer of Fe^{3+} to Fe^{2+} at the interface. On the basis of the polar catastrophe model, FeO_2/PbO interface is determined. First-principles calculation manifests that the oxygen vacancy at the interface plays a predominate role in inducing the local polarization enhancement. We propose a charge transfer mechanism that leads to the remarkable polarization increment at the $PbTiO_3/BiFeO_3$ interface. This study may facilitate the development of nanoscale ferroelectric devices by tailing the coupling of charge and lattice in oxide heteroepitaxy.

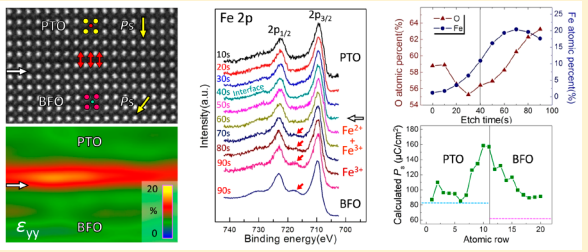

KEYWORDS: *Perovskite oxide, ferroelectric, interface, polarization enhancement, aberration corrected scanning transmission electron microscope*

Ferroelectrics featuring electrically switchable spontaneous polarizations are promising candidates for nanoscale microelectronic device, such as sensors, transducers, ultrathin ferroelectric capacitors, and ultrahigh density nonvolatile random access memories.[1,2] Although recent experiments have confirmed the presence of ferroelectricity in ultrathin films with the thicknesses down to one nanometer scale,[3,4] it is widely accepted that the interface-induced depolarization effects weaken the polarizations of ferroelectric films/interfaces,[5−13] which largely hampers the integrations of ferroelectrics into electronic devices (where interfaces are inevitable) and consequently hinders the utility of ferroelectrics. Thus, polarization enhancement at ferroelectric interfaces is of technological importance for facilitating the development of ferroelectrics-based electronic devices. Although recent first-principles calculations indicate that enhanced ferroelectricity could be achieved at the interface between AO-terminated ferroelectrics ($BaTiO_3$ and $PbTiO_3$) and simple metal (Pt, Au) through chemically modified stiffness of the ferroelectric−electrode bond,[14] the polarization enhancement at ferroelectric/ferroelectric interfaces has not been realized in experiments up to date.

Here we demonstrate an interfacial polarization enhancement driven by the charge transfer at oxide interfaces where discontinuities of both chemical valence and ferroelectric polarization are involved. Complex oxide interface engineering becomes a subject of great interest nowadays primarily driven by the first discovery of unexpected conduction and magnetism at the interface between two nonmagnetic insulating oxides. Among these heteroepitaxial systems, a typical example is the $LaAlO_3/SrTiO_3$ heteroepitaxy that exhibits a valence discontinuity.[15−18] In 2004, Ohtomo and Hwang demonstrated that the interfacial stacking sequence plays a critical role in determining the physical properties in this valence-discontinuous film system: a $Sr^{2+}O^{2-}/Al^{3+}O_2^{4-}$ interface is insulate, while a $Ti^{4+}O_2^{4-}/La^{3+}O^{2-}$ interface is able to generate highly mobile

Received: February 22, 2017
Revised: May 19, 2017
Published: May 25, 2017

DOI: 10.1021/acs.nanolett.7b00788
Nano Lett. 2017, 17, 3619−3628

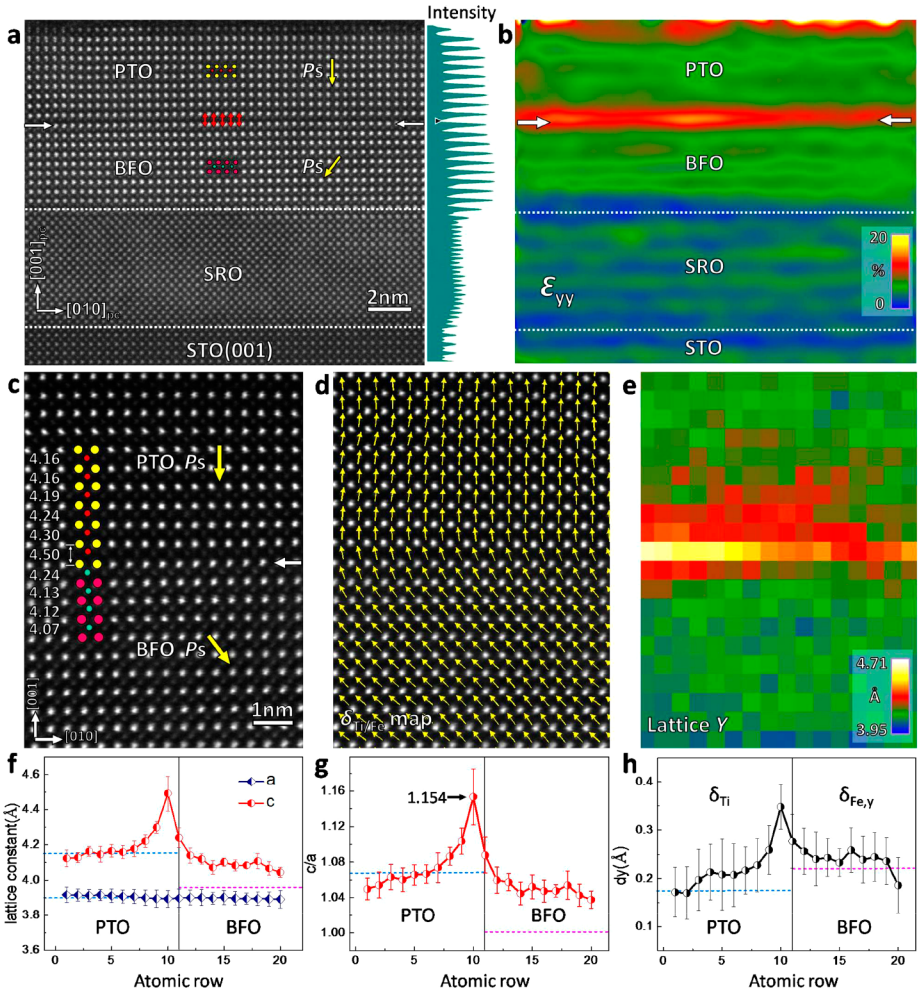

Figure 1. Lattice parameters, strain, and ion displacements of the $BiFeO_3/PbTiO_3$ film. (a) A HAADF-STEM image showing an atomic mapping of the $PbTiO_3$(~10 u.c.)/$BiFeO_3$/$SrRuO_3$ films grown on $SrTiO_3$ (001). The polarization directions in both $PbTiO_3$ and $BiFeO_3$ point to $SrRuO_3$ as indicated by yellow arrows. Double-headed red arrows indicate lattice elongation along out-of-plane direction. Intensity profile shows a remarkable low value as indicated by small black arrow, which corresponds to the layer with apparent lattice elongation. (b) GPA analysis of out-of-plane normal strains. (c) A HAADF-STEM image of the $PbTiO_3/BiFeO_3$ interface and the corresponding (d) $\delta_{Ti/Fe}$ map; (e) out-of-plane lattice spacing map; (f) in-plane (*a*, navy blue) and out-of-plane (*c*, red) lattice spacing profiles; (g) tetragonality profile; (h) out-of-plane displacement curve of Ti/Fe, where *dy* ($\delta_{Ti}/\delta_{Fe,y}$) is defined in Figure S1. White dashed lines and white arrows in images (a–c) indicate heterointerfaces. Numbers labeled in the image (c) indicate the lattice spacing (unit: Å).

two-dimensional (2D) electron gas.[16] Although the mechanism behind these behaviors is still under debate,[19,20] valence discontinuity induced electronic (oxygen vacancy, valence change of metal ions or spontaneous polarization in nonpolar oxides) and structural reconstruction (cation disorder) at the interface is believed to be the primary cause.[20−26] Besides valence discontinuity, ferroelectric polarization discontinuity leading to distinct interfacial properties has also been verified. The up and down polarization directions have been proved to result in the remarkable difference of both interfacial conductivity and magnetoelectric coupling.[27−30] Moreover, it is demonstrated that superlattices and bilayered films composed of two ferroelectrics with different polarization directions may give rise to an enhancement of electromechanical and dielectric properties.[31,32] Several studies on $BiFeO_3/BaTiO_3$ films also suggest a large magnetoelectric coupling at the interface.[33−37] Theoretically, $BiFeO_3/PbTiO_3$ superlattices have also been studied in a few works,[38,39] where strain-induced structural evolutions and the impact of interface polarity on ferroelectric behavior are investigated, yet none of dedicated experiments have been conducted. The integrated effects by considering both valence and ferroelectric polarization discontinuities on interfacial polarization behavior between two ferroelectrics displaying different polar directions and magnitudes are known little so far, though it is intuitive to believe that this combination behavior should be different from that of ferroelectric/electrode interfaces, and polarizations without damping are expected.

In this work, to experimentally investigate the interface behavior between oxides with both valence and ferroelectric polarization discontinuities, ferroelectric $PbTiO_3$ (PTO) and multiferroic $BiFeO_3$ (BFO) heterojunctions are designed and grown by pulsed laser deposition (PLD) on $SrTiO_3$ (STO) (001) substrates with a $SrRuO_3$ (SRO) buffer layer of 13 u.c. in thickness. Here, u.c. is the abbreviation of unit cell. The large ionic displacement in both PTO and BFO enables a direct extraction of spontaneous polarization (P_s) based on the advanced aberration-corrected scanning transmission electron microscopic (STEM) images. The SRO buffer layer is predeposited to make sure the polarization direction in BFO

DOI: 10.1021/acs.nanolett.7b00788
Nano Lett. 2017, 17, 3619−3628

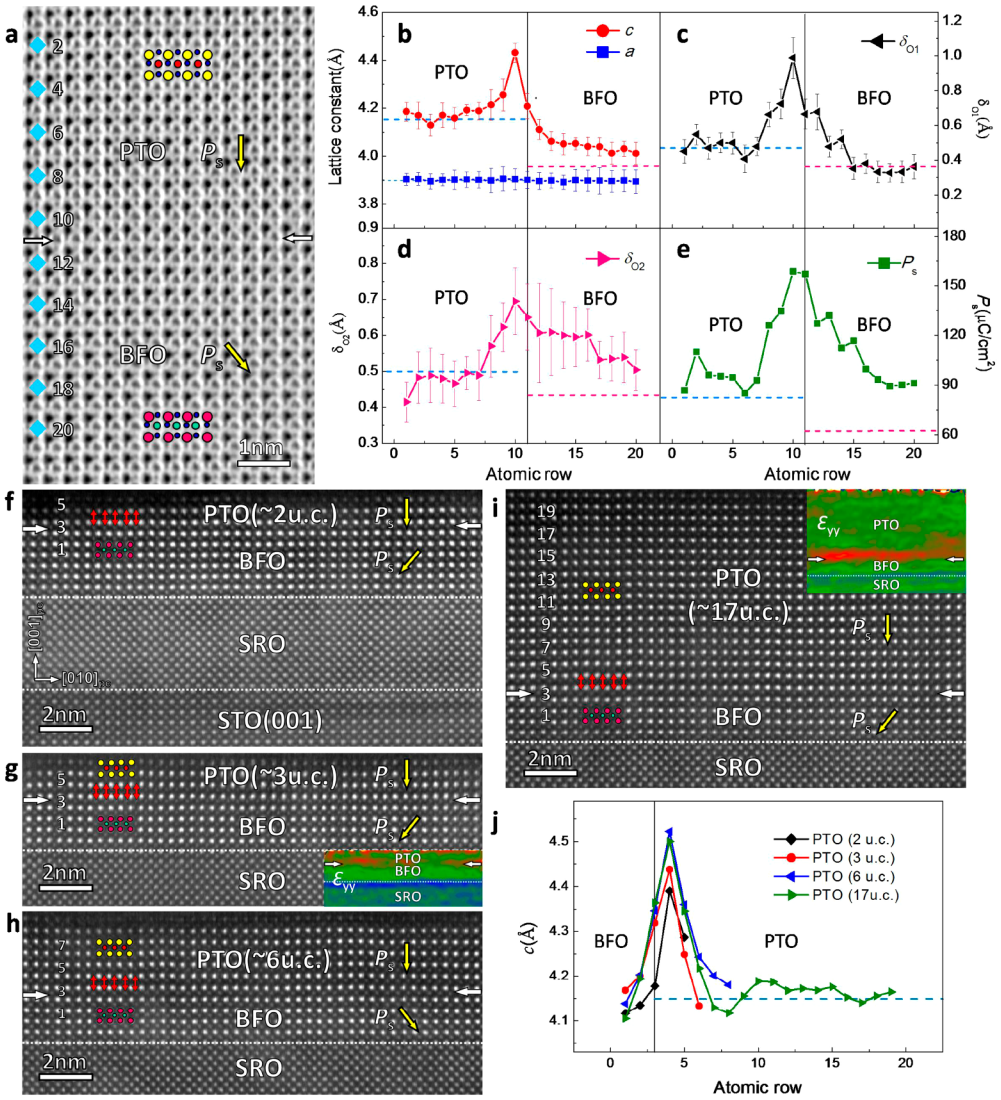

Figure 2. ABF-STEM imaging of $BiFeO_3/PbTiO_3$ interfaces and interfacial structural evolutions versus $PbTiO_3$ thickness. (a) Atomic resolved ABF-STEM image and (b) the corresponding in-plane and out-of-plane lattice parameters curves; (c,d) δ_{O1} and δ_{O2} profiles, where δ_{O1} and δ_{O2} are defined in Figure S1; (e) P_s curve calculated on the basis of in-plane, out-of-plane lattice constants, Ti/Fe and O atomic displacements in Figure 1h and panels b–d. The corresponding atomic rows are labeled as blue diamonds and numbers in the image of panel a. Atomic-resolved HAADF-STEM images for $PbTiO_3/BiFeO_3/SrRuO_3/SrTiO_3$ systems with different $PbTiO_3$ thicknesses: (f) 2 u.c., (g) 3 u.c., (h) 6 u.c. and (i) 17 u.c.. The insets in (g,i) show the corresponding GPA analyses of out-of-plane normal strains. out-of-plane lattice parameters c extracted from these HAADF-STEM images are shown in (j). The increases of the out-of-plane lattice parameters in the first unit cell of $PbTiO_3$ layers near the $BiFeO_3/PbTiO_3$ interface are remarkable. Here, error bars are omitted in order to clearly present the values in the curves. Yellow arrows in (a,g) indicate P_s directions. Blue and pink dashed lines in (b–e,g) denote the corresponding bulk values.

pointing toward the substrate (determined by the difference in work function). By a combination of high-angle annular dark-field (HAADF) imaging, annular bright-field (ABF) STEM imaging, electron energy loss spectrum (EELS), and X-ray photoelectron spectroscopy (XPS) depth analysis, we investigate charge compensation at the BFO/PTO interface, which is responsible for a remarkable enhancement of ferroelectric polarizations.

Ferroelectric PTO has a tetragonal unit cell in which both Ti and the oxygen octahedron have a displacement from the center of its four nearest Pb, giving rise to the spontaneous polarization along [001] direction. BFO exhibits a distorted perovskite structure with rhombohedral symmetry where Fe shifts slightly from the body center of pseudocubic structure along $\langle 111 \rangle_{pc}$ directions and six oxygen atoms forms a distorted octahedron. For simplicity, BFO is regarded as a pseudocubic structure in the present study. The atomic projections of PTO and BFO along $[100]_{pc}$ are schematically shown in Figure S1. For both PTO and BFO unit cells, the shift directions of Ti (denoted as δ_{Ti}) and Fe (denoted as δ_{Fe}) are used to determine the polarization directions and they are opposite to the ferroelectric spontaneous polarizations.[10,40,41]

A high-resolution HAADF-STEM image of the film system is shown in Figure 1a where the PTO/BFO interface is marked with a pair of opposite white arrows. PTO (~10 u.c.)/BFO (~10 u.c.) was grown on a STO (001) substrate with SRO (~13 u.c.) as a buffer layer. The heteroepitaxial interface is very sharp and the film surface is atomically flat (as seen in Figure S2). In the HAADF images of BFO/PTO film, Pb and Bi columns appear to be the brightest, while Ti and Fe show weaker brightness owing to the fact that the intensity in HAADF image is approximately proportional to $Z^{1.6-1.9}$ (refs 42

DOI: 10.1021/acs.nanolett.7b00788
Nano Lett. 2017, 17, 3619–3628

and 43.). The polarization directions of PTO and BFO are determined by Ti and Fe displacements, respectively, basically pointing to the STO substrate as indicated by yellow arrows. It is of great interest to note that an elongation of the out-of-plane lattice spacing appears at BFO/PTO interface as denoted with vertical double-head red arrows. Intensity profile of the image (shown in the right of the experimental images) displays a remarkable valley as indicated by a small black arrow, which corresponds to the layer with apparent lattice elongation. To directly visualize this variation, geometric phase analysis (GPA) based on the HAADF-STEM image is performed along in-plane and out-of-plane directions, as shown in Figures S3 and 1b, respectively. It is seen that the in-plane strain (Figure S3) is homogeneous, indicating the fully epitaxial growth of the film system; while the out-of-plane strain (Figure 1d) manifests an abrupt change at the interface, which is deduced to be a ∼15% tensile strain along the out-of-plane direction compared with the STO substrate.

To figure out the atomic details of this unusual BFO/PTO interface phenomenon, atomically resolved STEM imaging is performed and shown in Figure 1c. The atomic column positions in this image are determined by two-dimensional Gaussian fitting[39,44,45] and the averaged lattice spacing between neighboring Pb rows is labeled as numbers in the image. Expansions of the out-of-plane lattice spacing occur around the PTO/BFO interface and a maximal expansion appears at the interface, reaching a value of as high as 4.50 Å and implying a huge polarization at the interface.[10,46] To directly visualize the polarization distribution, Ti/Fe displacements relative to Pb/Bi ($\delta_{Ti/Fe}$) are extracted unit cell by unit cell (the details can be found in Supporting Information and Figure S4) and shown in Figure 1d. Such displacements are opposite to the PTO/BFO polarization directions. Extractions of lattice parameters on the basis of HAADF-STEM image provides more information on the polarization strength. Figure 1f is the out-of-plane lattice spacing map of Figure 1c. The obvious elongation along the out-of-plane direction can be identified with a local maximum of 4.71 Å. The in-plane and out-of-plane lattice spacing profiles averaged over each row are shown in Figure 1g, in which a peak value (about 4.5 Å) of out-of-plane lattice spacing is observed near the interface, while the in-plane lattice spacing over the whole region remains uniform. Here, the lattice parameters of bulk PTO are c = 4.153 Å and a = 3.899 Å as indicated by dotted lines at the PTO side, while the lattice constant of bulk BFO is 3.965 Å as denoted by a dotted line at the BFO side. Based on the data shown in Figure 1g, the tetragonality of c/a is derived and a peak value of approximately 1.15 is observed (shown in Figure 1h). Here, the blue and pink dashed lines correspond to the values of c/a in bulk PTO and BFO, respectively. Such a peak value for c lattice may indicate a polarization enhancement at the interface since the spontaneous polarizations in ferroelectric PTO are strongly coupled with spontaneous strains (or teetragonality).[10,46] To further identify the polarization distributions across the interface, averaged Ti/Fe displacement profile along out-of-plane (dy, as defined in Figure S1) is shown in Figure 1i. Similarly, an apparent increase of dy is observed near the BFO/PTO interface which is much larger than that of bulk PTO (0.17 Å) and BFO (0.24 Å), respectively. The maximums of both lattice and ferroelectric displacements at the BFO/PTO interface strongly support a local polarization enhancement near the interface.

We use a phenomenological approach and estimate the potential ferroelectricity enhancement near the interface. On the basis of the Landau−Ginzburg−Devonshire theory, ferroelectric polarization can be calculated by the equation shown below[47,48]

$$P_s = \left(\frac{x_s - \frac{2s_{12}x_m}{(s_{11}+s_{12})}}{Q_{11} - \frac{2s_{12}Q_{12}}{(s_{11}+s_{12})}} \right)^{1/2} \quad (1)$$

In this equation, $x_3 = (c - a_p)/a_p$; $x_m = (a - a_p)/a_p$; a and c are in-plane and out-of-plane lattice parameters; a_p, lattice parameter of cubic PTO being extrapolated to room temperature; s_{ij}, elastic compliances; Q_{ij}, electrostrictive coefficients. The values of a_p, Q_{ij}, and s_{ij} for PTO are adopted from refs 40 and 49. The calculated P_s for the largest averaged c value in PTO is 142 μC/cm^2. This is ∼70% larger than that in the bulk (∼83 μC/cm^2, derived also from the equation above).

It is worthwhile to mention that although phenomenological approach based on the Landau−Ginzburg−Devonshire theory is proved to be effective in estimating ferroelectric behaviors, it does not take into account of the atomic and electronic information to address the polar behaviors.

To comprehensively demonstrate the local polarization enhancement at the PTO/BFO interfaces, we also apply the ABF-STEM imaging technique, which is powerful for imaging O atom columns. As seen in the ABF-STEM images (Figure 2a), the darkest spots indicate Pb and Bi, whereas dark image spots with weak contrast correspond successively to Ti, Fe, and O. The atomic projection along $[100]_{pc}$ for both PTO and BFO is superimposed on the ABF image. On the basis of the ABF-STEM image, we extract the in-plane and out-of-plane lattice parameters (a and c) along the route across the BFO/PTO interface, and the results are shown in Figure 2b. It is clear that the variations are similar to those extracted from HAADF image shown in Figure 1f. It is noted that in-plane "a" is quite the same of about 3.9 Å for both BFO and PTO layers because they are clamped by the STO substrate, while out-of-plane lattice parameters "c" show remarkable enhancements near the BFO/PTO interface, matching well with those extracted from the HAADF image in Figure 1c. Furthermore, O1 and O2 displacements (δ_{O1} and δ_{O2}, defined in Figure S1) are extracted and the corresponding curves are shown in Figure 2c,d, respectively. Significant increases of δ_{O1} and δ_{O2} at the BFO/PTO interface are revealed, which are as large as 0.99 and 0.69 Å, respectively. To better display such a difference, the corresponding values (δ_{O1} and δ_{O2}) in bulk PTO of 0.48 and 0.5 Å are indicated with the light blue lines; simultaneously, the values in bulk BFO are 0.36 and 0.42 Å as indicated with the pink lines in Figure 2c,d. Figure 2e is a profile showing the calculated polarizations along out-of-plane direction, and it further verifies the polarization enhancement at the interface, where a polarization as large as 158 μC/cm^2 is revealed, which is about 90% larger than that in bulk PTO. Here, P_s are derived from lattice parameters of a and c, Ti/Fe, and oxygen displacements ($\delta_{Ti/Fe}$, δ_{O1}, and δ_{O2}), as well as Born effective charges. The P_s values of PTO/BFO are calculated based on the equation[50,51] shown below

$$P_s = \frac{e}{V} \sum Z_i^* \delta_i \quad (2)$$

where $e = -1.6 \times 10^{-19}$C and refers to electron charge; V is the volume of PTO or BFO unit cell; Z_i^* is Born effective charge of

DOI: 10.1021/acs.nanolett.7b00788
Nano Lett. 2017, 17, 3619−3628

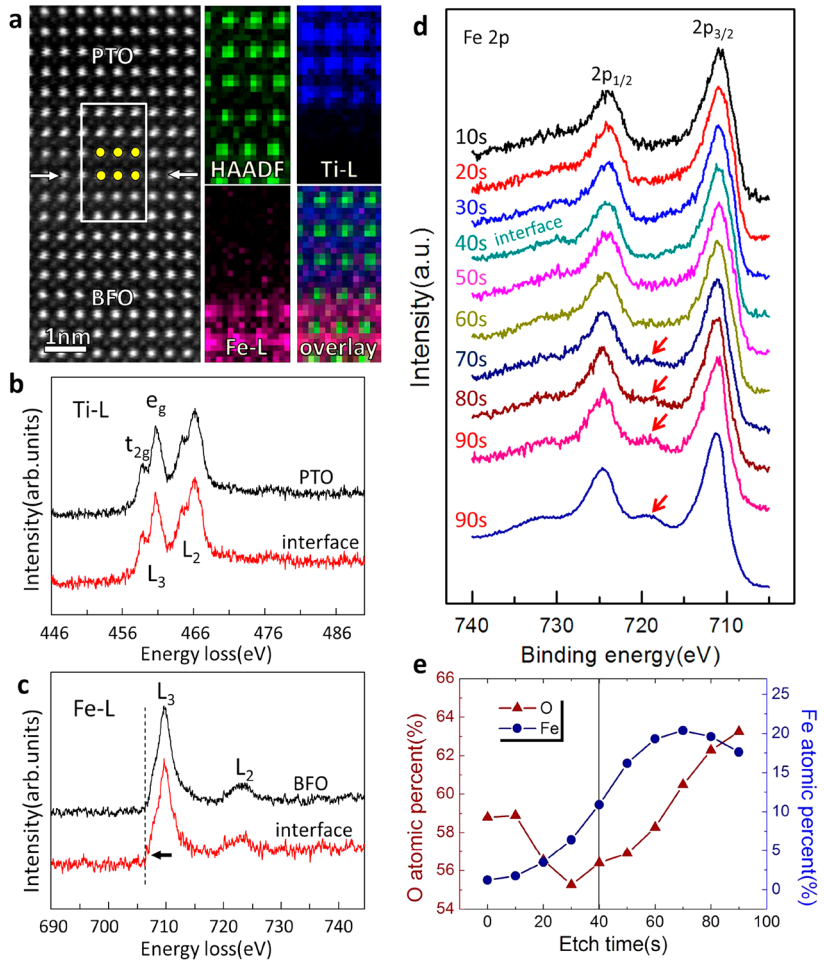

Figure 3. Electron energy loss spectrum and X-ray photoelectron spectroscopy analysis of the $BiFeO_3/PbTiO_3$ interface with 10 u.c. thick PTO. (a) HAADF-STEM image and EELS chemical maps of Ti and Fe for the rectangular area. The bright spots in yellow indicate Pb or Bi. (b) Ti EEL spectrum for $PbTiO_3$ film and the interface. (c) Fe EEL spectrum from $BiFeO_3$ film and interface. (d) Fe X-ray photoelectron spectra with different etch time. (e) O and Fe depth profiles as a function of etch time.

atom *i* (Born effective charge of PTO is adopted from ref 51 and that of BFO is calculated by ab initio; the details of calculation can be found in Supporting Information); δ_i is off-center displacement of atom *i*. δ_{O1} and δ_{O2} are extracted from the ABF images whereas $\delta_{Ti/Fe}$ is extracted from HAADF image in Figure 1c (Ti and Fe displacements are not extracted from ABF-STEM image in Figure 2a, because they are overlapped with O in this image and hence less accurate than that extracted from HAADF image).

The calculated out-of-plane spontaneous polarizations in BFO layer demonstrate that they are also dramatically enhanced compared with the corresponding bulk value (62 $\mu C/cm^2$, along out-of-plane direction, as indicated by the pink dashed line), and this enhancement is particularly significant at the position about four unit cells away from the BFO/PTO interface. In addition, P_s in BFO far away from the interface is also remarkably enhanced, which is supposed to be induced by the in-plane compressive strain exerted by the STO substrate.

In order to gain insight into the size-dependent enhancement of polarization at the interfaces, we have grown a series of PTO/BFO/SRO multilayered films on STO (001) with the thicknesses of PTO ranging from 2 to 6 u.c., smaller and also larger (17 u.c.) than that shown above (~10 u.c.). The HAADF images of these films are shown in Figure 2f–i from which significant lattice elongation is extensively observed and indicated by red double-head arrows. The corresponding out-of-plane lattice parameters (*c*) are extracted and shown in Figure 2j. From Figure 2j, an obvious increase of *c* is revealed near the BFO/PTO interfaces in all of the four films, suggesting a remarkable enlargement of polarization along out-of-plane direction near the PTO/BFO interfaces since the strong coupling of ferroelectricity and spontaneous strains (or tetragonality) of PTO.[10,46] For 6 u.c. and 17 u.c. thick PTO, the largest *c* reaches 4.5 Å, comparable with that of 10 u.c. thick PTO shown above; when further decreasing PTO thickness, the peak values *c* decrease a little to 4.44 and 4.39 Å for 3 u.c. and 2 u.c. thick PTO, respectively. These values are still remarkably enhanced compared with the corresponding bulk value (4.153 Å).

To seek for the physical insight induced by the chemical discontinuity at the BFO/PTO interface, the chemical and electronic information are further investigated. We apply EELS approach on the basis of the atomic level HAADF-STEM of the BFO(10 u.c.)/PTO(10 u.c.) interface (as seen Figure 3a–c). The Ti and Fe elemental maps in Figure 3a show that TiO_2 is at the elongation layer, while its adjacent layer toward the substrate is FeO_2. From the Ti elemental map, an abrupt BFO/PTO interface is derived. The slight noise in the PTO layer of the Fe elemental map is proposed to be a result of relatively low intensity of Fe-L peak compared with that of Ti-L, particularly

DOI: 10.1021/acs.nanolett.7b00788
Nano Lett. 2017, 17, 3619–3628

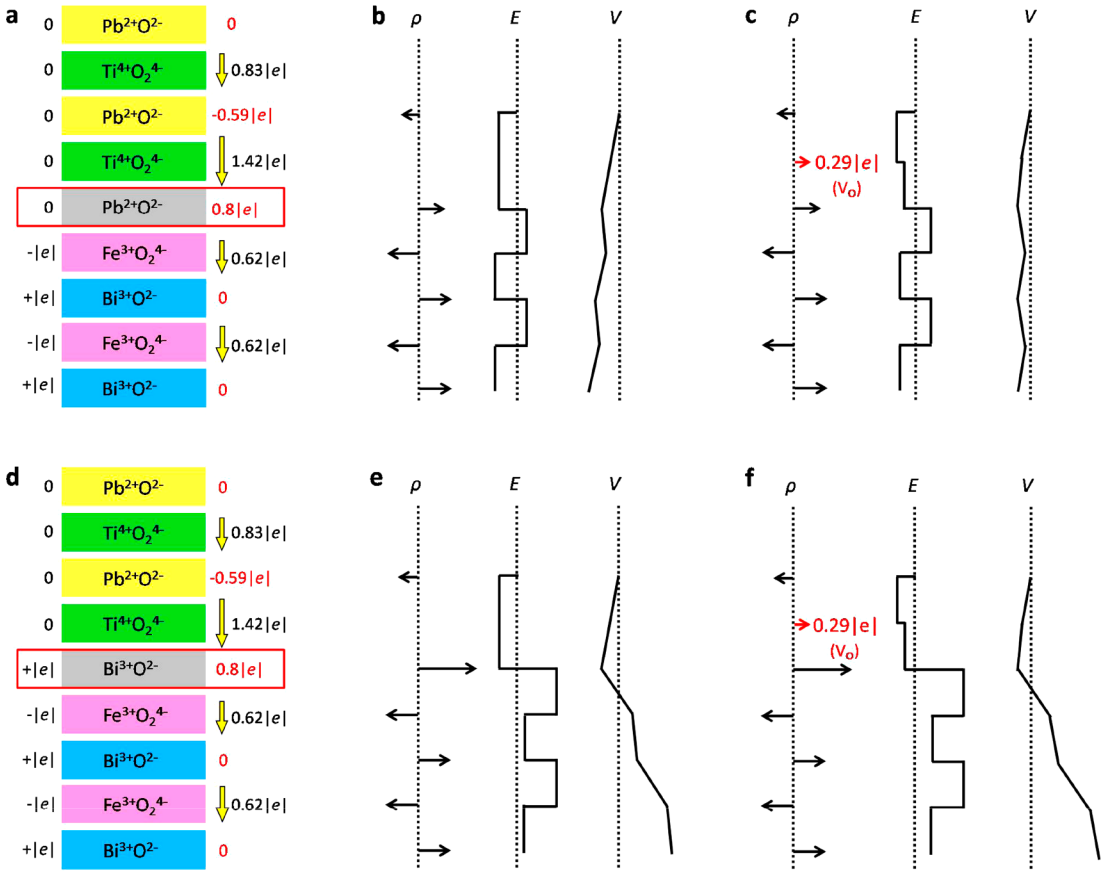

Figure 4. Interfacial charge reconstructions for FeO_2/PbO and BiO/TiO_2 interfaces. (a) A schematic illustration of FeO_2/PbO interface. (b) Charge reconstruction when considering the discontinuity of both valence and ferroelectric polarization (ρ, net charges; E, electric field; V, electric potential). The negative shift of E results in an electric potential diverging with thickness. (c) The polarization catastrophe is avoided if considering not only valence and ferroelectric polarization discontinuities but also oxygen vacancy. (d) A schematic of BiO/TiO_2 interface. (e,f) The electric potential unavoidably diverges for the BiO/TiO_2 interface regardless of whether oxygen vacancies are taken into account or not.

at a high spatial resolution. The valence states of both Ti and Fe are probed by atomic scale EELS and shown in Figure 3b,c, respectively. The energy resolution here is 0.5 eV evaluated from the full width of zero loss peak at half-maximum. The Ti-L_3 edge (Figure 3b) energy splitting is detected to be ~1.82 eV, which is a little larger than 1.65 eV reported for bulk PTO (ref 52) and smaller than that for bulk STO and $BaTiO_3$,[53,54] perhaps due to a little deviation from bulk symmetry. The Ti-L EEL spectrum fingerprint provides no obvious difference between BFO/PTO interface and PTO film, which suggests that no remarkable valence change occurs for Ti. The Fe-L energy edge EELS spectrum is shown in Figure 3c. Fe-L_3 energy edge reveals a general trend of shifting left and toward lower energy-loss value at the BFO/PTO interface. Particularly, at the right side of the black dotted line, the relative height of the EELS curve at the interface is obviously larger than that of the BFO layer, which implies a decrease of oxidation state from Fe^{3+} to Fe^{2+} (ref 55).

To further verify this valence change of Fe near the interface, we conduct measurements based on X-ray photoelectronic spectroscopy (XPS), which is more valence-sensitive. We probed the film layer by layer (Figure S5), and monitored the variety of element composition and valence information versus the depth of etching (Figure 3d,e). The etch rate is ~0.1 nm/s, taking Ta_2O_5 as a measuring standard. According to the film thickness and the etch rate, it is assumed that the interface is at the position after the film was etched for 40s. According to previous reports,[56,57] the position of Fe $2p_{3/2}$ peak should be at 709.5 eV for Fe^{2+} and 711 eV for Fe^{3+}; while the Fe^{3+} satellite peak should be at 719 eV and Fe^{2+} satellite peak at 716 eV. Figure 3d shows a sequence of Fe-2p XPS with BFO/PTO film being etched gradually from 10 to 90 s. From these spectra, we identify that, as the film is etched from 10 to 40 s, Fe XPS signals show relatively high intensity at Fe^{2+} (716 eV) and low intensity at Fe^{3+} (719 eV) satellite peak positions. Fe^{2+} or Fe^{3+} satellite peak is not observed between Fe $2p_{3/2}$ and Fe $2p_{1/2}$ in the 10−40 s spectra. This is consistent with the spectrum of Fe^{2+} and Fe^{3+} mixture, as observed in Fe_3O_4 (ref 58). When the etch time increases to 50−60 s, the intensity difference between Fe^{2+} and Fe^{3+} satellite peak becomes smaller (50 s) and then almost equivalent (60 s). This indicates that the component of Fe^{3+} gradually increases. As the etch time is increased to 70s, the Fe^{3+} satellite peak appears at 719 eV, as marked with red arrows. These results suggest that Fe^{2+} and Fe^{3+} coexist at the BFO/PTO interface, while Fe features +3 valence in the BFO film. Here, two reasons can be ascribed to the formation of Fe^{2+} near the BFO/PTO interface. One is to reduce the band offset at the BFO/PTO interface, as suggested by Nakagawa et al.[21] for the $LaAlO_3$/$SrTiO_3$ interface where the polar discontinuity is similar to that in our present study. The other is the inhomogeneous polarizations in the BFO layer near the interface. The downward polarization in BFO near the BFO/PTO interface is larger than that far away from the BFO/PTO interface as deduced in Figure 2e, and hence the polarization

DOI: 10.1021/acs.nanolett.7b00788
Nano Lett. 2017, 17, 3619−3628

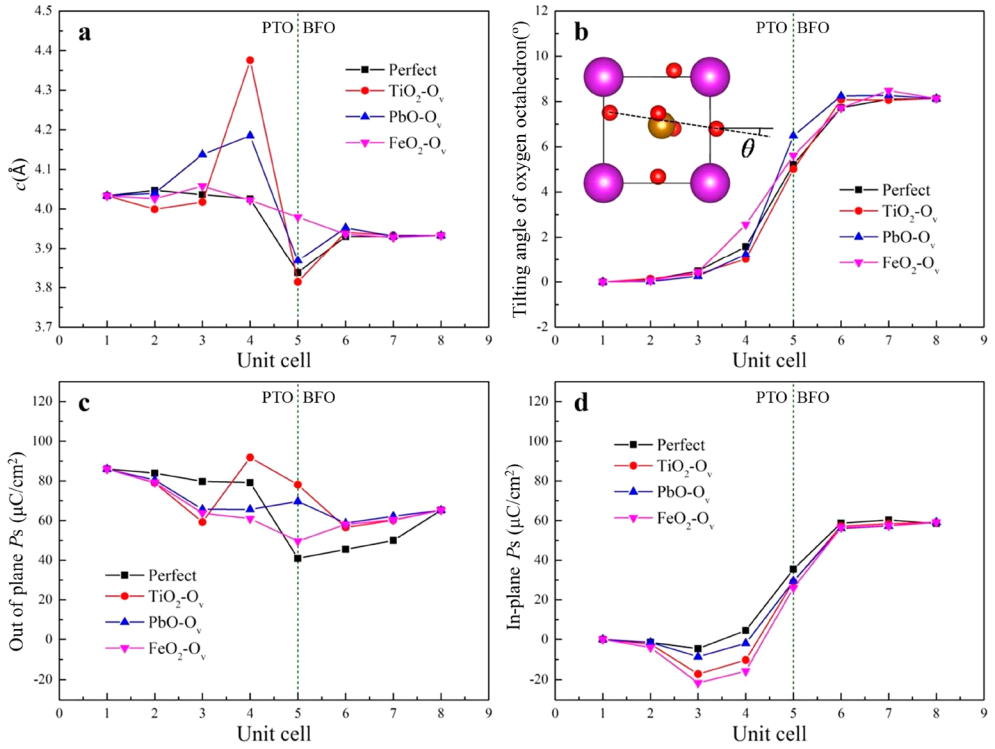

Figure 5. Results from first-principles calculations for different atomic planes with oxygen vacancy accumulations. (a) Lattice parameter *c*. (b) Averaged [100] and [010] axial tilt angles. (c) [001] polarization component P_z. (d) Averaged [100] and [010] polarization component $P_{x,y}$. The green dot line denotes the location of the $BiFeO_3/PbTiO_3$ interface.

difference may lead to the positive bound charges near the interface (shown in Figure S6), which can be compensated via the reduction of Fe valence from Fe^{3+} to Fe^{2+}.

The depth profiles of Fe and O as shown in Figure 3e manifest the composition change as a function of etching time (or the depth of film). The profile of Fe atomic percent shows a clear increase as the film was etched from 0 to 70 s. When the film was etched for 40 s, the gradient displays the largest, which corresponds to the BFO/PTO interface. In addition, it is worth noting that O atomic percent profile shows a trend of decrement from 59% (not etched) to 55% (etched for 30 s) and then an increase to 63% (etched for 90 s). These results imply that oxygen vacancy is involved at the BFO/PTO interface, suggesting that oxygen vacancy be responsible for the remarkable elongation of out-of-plane lattice spacing and the large spontaneous polarization in PTO near the BFO/PTO interface (oxygen vacancy induced lattice elongation is widely observed in perovskite oxides[59,60]).

In addition to these factors such as the P_s discontinuity, valence changes of Fe and Oxygen vacancy accumulations at the BFO/PTO interface, we propose that the interfacial termination layer may also play a significant role in the polarization enhancement. This is because the difference in charge distributions between $(FeO_2)^-/(PbO)^0$ and $(BiO)^+/(TiO_2)^0$ interfaces enables contrasting charge compensation mechanisms.[21,61] Generally, PTO exhibits an alternating stacking of neutral $(PbO)^0$ and $(TiO_2)^0$ planes along [001] direction, whereas BFO features an alternating stacking of polar $(BiO)^+$ and $(FeO_2)^-$ planes. At a BFO/PTO (001) interface, two stacking configurations, namely FeO_2/PbO and BiO/TiO_2, may arise and both feature a polar discontinuity. Because Pb and Bi atoms are difficult to be distinguished from both EDS and EELS analyses, the interfacial termination layer cannot be directly determined in experimental observations. Alternatively, we propose a simplified model based on the polar catastrophe to qualitatively rationalize the interfacial stacking sequence (Figure 4).

Figure 4a is a schematic illustration showing the $(FeO_2)^-/(PbO)^0$ stacking sequence across the interface. To facilitate the interpretation, valences of "1−", "1+" and "0" are converted to the corresponding charge values and labeled as $-|e|$/u.c., $+|e|$/u.c., and 0, respectively, on the left side of Figure 4a. In addition to the charge distribution caused by nonzero valence, ferroelectric polarization discontinuity may also give rise to a net charge accumulation at the interface. As seen in Figure 2k, the P_s profile shows maximum in the first unit cell of PTO layer at BFO/PTO interface, and the P_s values away from the interface decrease gradually to the value of the bulk. For the sake of simplicity, except for the largest P_s value in PTO (142 $\mu C/cm^2$, derived from phenomenological theoretical calculations above; the exact interface is not considered here since it deviates from the bulk BFO and PTO, and this simplified process does not influence our results), P_s values in both BFO and PTO are assumed to be the bulk values of 62 $\mu C/cm^2$ for BFO (along out-of-plane direction) and 83 $\mu C/cm^2$ for PTO. To clearly display and compare the charge variations caused by both ferroelectric polarization and valence difference, the P_s is expressed with the same unit as that of valence-induced charge via the following transformational relationship

$$1\ \mu C/cm^2 = 1 \times 10^{-22}\ C/A^2 = 1 \times 10^{-22} \times 3.9^2\ C/u.c. = 1.6 \times 10^{-21}\ C/u.c. = 0.01|e|/u.c. \quad (3)$$

In this equation, "3.9" is in-plane lattice constant for both PTO and strained BFO, whose unit is angstroms.

DOI: 10.1021/acs.nanolett.7b00788
Nano Lett. 2017, 17, 3619−3628

The P_s with the value of 142 uC/cm^2, 83 uC/cm^2 and 62 uC/cm^2 are approximately translated to be 1.42|e|/u.c., 0.83|e|/u.c., and 0.62|e|/u.c., respectively. These values are labeled on the right side of Figure 4a. Because the continuous polarization keeps the charge neutral, the polar-induced net charge in both BFO and PTO layers far away from interface is assumed to be zero. Net charges near the interface are calculated using the polar difference in adjacent unit cells and are labeled in red. On the basis of these data, the total net charge of ρ, which is a sum of charges resultant from both valence and polar discontinuity, is shown in Figure 4b where the corresponding electric field (E) and electric potential (V) are also displayed. In these schematics, vertical dashed lines indicate the zero value of physical parameters (ρ, E, V). On the left of these lines, ρ, E, and V have a negative value while in the right side, they show positive. Direction and length of the arrows in ρ represent its sign (positive or negative) and magnitude, respectively. On the basis of this distribution map, E and V can be deduced. It is noted that the electrical potential tends to diverge from the zero plane when the stacking plane goes from PTO layer to BFO layer and no convergence can be expected, implying a polarization catastrophe. However, if charged oxygen vacancy of 0.29|e|/u.c. is introduced as shown in Figure 4c, electronic potential becomes convergent and a polar catastrophe can be avoided. Here, we assume that oxygen vacancy lies at TiO_2 layer where the lattice is obviously elongated as indicated by the red arrow in Figure 1b. The charge of oxygen vacancy is calculated to be ρ_{Vo} = (0.5−0.8 + 0.59)|e|/u.c. = 0.29|e|/u.c., according to the half electron transfer model which may avoid potential divergence as reported previously for $LaAlO_3/SrTiO_3$ interfaces.[21]

For the BiO/TiO_2 interface, similar analysis is carried out and shown in Figure 4d−f. This stacking sequence leads to a positively charged interface, namely $(BiO)^+/(TiO_2)^0$. Moreover, when ferroelectric polarization discontinuity is taken into account, the large polarization in PTO compared with BFO further aggravates positive charge accumulations (0.8|e|/u.c.) at the interface. The large accumulation of positive charges eventually results in a potential divergence toward positive electric potential as shown in Figure 4e. This is in contrast to the divergence toward negative for FeO_2/PbO interface shown in Figure 4b. When the oxygen vacancy is also introduced with the same amount as that for FeO_2/PbO interface, the divergence turns worse, excluding the possibility of BiO/TiO_2 as the terminated layer.

To further rationalize the polarization enhancement near the BFO/PTO interface (FeO_2/PbO), we performed first-principles calculations. Details of the calculation are shown in the Supporting Information. The $[BFO]_5/[PTO]_5$ (001) slabs with FeO_2/PbO interface are built according to our experimental results, and the models are shown in Figure S7a. In order to judge the site preference of oxygen vacancy, we calculate slabs with the oxygen vacancy at the TiO_2 (Figure S7b), PbO (Figure S7c), and FeO_2 (Figure S7d) (001) atomic planes, which are labeled as TiO_2-O_v, $PbO-O_v$, and FeO_2-O_v, respectively. The slabs without oxygen vacancy accumulations are defined as perfect. The calculated results are shown in Figure 5. The out-of-plane lattice parameter c profiles shown in Figure 5a reveal a low value of c at the exact interface for the perfect BFO/PTO model. When oxygen vacancies are introduced onto TiO_2 and PbO atomic planes, the c values increase rapidly which reach as high as 4.375 and 4.18 Å in the first PTO unit cell, respectively. The oxygen octahedral distortion/tilt and displacements in perovskite oxides are known to play significant roles in determining the functionalities like magnetic, electric and ferroelectric polarization.[50,62,63] Here, the in-plane averaged tilt angles θ of the oxygen octahedra are extracted and shown in Figure 5b, where θ is defined in the inset. From these θ curves, it can be identified that tilt angles of oxygen octahedrons in PTO near the perfect interface reach a value of 1.6°, which are slightly reduced by the TiO_2-O_v and $PbO-O_v$ but enhanced up to 2.6° by the FeO_2-O_v. The oxygen octahedron behaviors indicate that structures of both PTO and BFO are not changed greatly (except for the exact interface). The [001] polarization component P_z and the averaged [100] and [010] polarization component $P_{x,y}$ are shown in Figure 5c,d, respectively. The P_z in PTO are slightly reduced with a tiny $P_{x,y}$ emerging near the interface. Both $PbO-O_v$ and FeO_2-O_v further reduce the P_z and enhance the $P_{x,y}$, however, the TiO_2-O_v remarkably enhances the P_z and $P_{x,y}$ up to 92 μC/cm^2 and 10 μC/cm^2, respectively. A combination of the calculated results and experimental observations indicates that the TiO_2-O_v and $PbO-O_v$ contribute to the observed out-of-plane tension strain, while only TiO_2-O_v benefits the P_z enhancement. Thus, the TiO_2-O_v takes predominant effect in the formation of out-of-plane tensile strain with enhanced P_z in PTO near the FeO_2/PbO interface.

In summary, we demonstrate a mechanism inducing remarkable enlargement of polarizations in BFO/PTO films. Particularly, a local enhancement of ferroelectric polarizations is revealed at the head-to-tail polarized interface, which results from oxygen vacancy accumulation at this chemical valence and ferroelectric polarization discontinuities. The FeO_2/PbO stacking sequence across the interface is derived on the basis of the polar catastrophe model. It is supposed that the FeO_2 termination and the downward ferroelectric polarizations in BFO layer result in the large negative charges accumulation at the BFO/PTO interface, which facilitate the formation of positively charged oxygen vacancy as well as the enhancement of ferroelectric polarization in PTO. First-principles calculations further verify the interfacial oxygen vacancy induced polarization enhancement. These results suggest that the ferroelectric polarizations at an epitaxial interface could be tuned by a controllable atomic arrangement across the interface. The results also extend the potential of engineering an interface at an atomic scale for developing nanoscale ferroelectric devices with exotic behaviors at the interface.

■ ASSOCIATED CONTENT

Supporting Information

The Supporting Information is available free of charge on the ACS Publications website at DOI: 10.1021/acs.nanolett.7b00788.

Details on thin film growth; TEM sample preparation, HAADF/ABF-STEM imaging, EEL spectrum and spectrum imaging; determination of atomic column positions and $\delta_{Ti/Fe}$ map; details of experimental data extraction; calculations of spontaneous polarizations based on the ABF image; X-ray photoelectron spectroscopy and depth profiling; and details of first-principles calculations on the BFO/PTO interface (PDF)

DOI: 10.1021/acs.nanolett.7b00788
Nano Lett. 2017, 17, 3619−3628

AUTHOR INFORMATION

Corresponding Authors

*E-mail: ylzhu@imr.ac.cn.

*E-mail: xlma@imr.ac.cn.

ORCID

Yin-Lian Zhu: 0000-0002-0356-3306

Notes

The authors declare no competing financial interest.

ACKNOWLEDGMENTS

This work is supported by the National Natural Science Foundation of China (Nos. 51231007, 51571197, 51501194, 51671194, and 51401212), National Basic Research Program of China (2014CB921002), and the Key Research Program of Frontier Sciences CAS (QYZDJ-SSW-JSC010). Y.L.T. acknowledges the IMR SYNL-T.S. Kê Research Fellowship and the Youth Innovation Promotion Association CAS (No. 2016177). The authors are grateful to B. Wu and L. X. Yang of this laboratory for their technical supports on the Titan platform of G2 60-300 kV aberration-corrected scanning transmission electron microscope.

REFERENCES

(1) Tsymbal, E. Y.; Kohlstedt, H. *Science* **2006**, *313*, 181−183.

(2) Scott, J. F. *Science* **2007**, *315*, 954−959.

(3) Bune, A. V.; Fridkin, V. M.; Ducharme, S.; Blinov, L. M.; Palto, S. P.; Sorokin, A. V.; Yudin, S. G.; Zlatkin, A. *Nature* **1998**, *391*, 874−877.

(4) Fong, D. D.; Stephenson, G. B.; Streiffer, S. K.; Eastman, J. A.; Auciello, O.; Fuoss, P. H.; Thompson, C. *Science* **2004**, *304*, 1650−1653.

(5) Tybell, T.; Ahn, C. H.; Triscone, J. M. *Appl. Phys. Lett.* **1999**, *75*, 856−858.

(6) Junquera, J.; Ghosez, P. *Nature* **2003**, *422*, 506−509.

(7) Lichtensteiger, C.; Triscone, J. M.; Junquera, J.; Ghosez, P. *Phys. Rev. Lett.* **2005**, *94*, 047603.

(8) Sai, N.; Kolpak, A. M.; Rappe, A. M. *Phys. Rev. B: Condens. Matter Mater. Phys.* **2005**, *72*, 020101.

(9) Gerra, G.; Tagantsev, A. K.; Setter, N.; Parlinski, K. *Phys. Rev. Lett.* **2006**, *96*, 107603.

(10) Jia, C. L.; Nagarajan, V.; He, J. Q.; Houben, L.; Zhao, T.; Ramesh, R.; Urban, K.; Waser, R. *Nat. Mater.* **2007**, *6*, 64−69.

(11) Chisholm, M. F.; Luo, W.; Oxley, M. P.; Pantelides, S. T.; Lee, H. N. *Phys. Rev. Lett.* **2010**, *105*, 197602.

(12) Huang, R.; Ding, H. C.; Liang, W. I.; Gao, Y. C.; Tang, X. D.; He, Q.; Duan, C. G.; Zhu, Z. Q.; Chu, J. H.; Fisher, C. A. J.; Hirayama, T.; Ikuhara, Y.; Chu, Y. H. *Adv. Funct. Mater.* **2014**, *24*, 793−799.

(13) Morozovska, A. N.; Eliseev, E. A.; Svechnikov, S. V.; Krutov, A. D.; Shur, V. Y.; Borisevich, A. Y.; Maksymovych, P.; Kalinin, S. V. *Phys. Rev. B: Condens. Matter Mater. Phys.* **2010**, *81*, 205308.

(14) Stengel, M.; Vanderbilt, D.; Spaldin, N. A. *Nat. Mater.* **2009**, *8*, 392−397.

(15) Ohtomo, A.; Muller, D. A.; Grazul, J. L.; Hwang, H. Y. *Nature* **2002**, *419*, 378−380.

(16) Ohtomo, A.; Hwang, H. Y. *Nature* **2004**, *427*, 423−426.

(17) Reyren, N.; Thiel, S.; Caviglia, A. D.; Kourkoutis, L. F.; Hammerl, G.; Richter, C.; Schneider, C. W.; Kopp, T.; Ruetschi, A. S.; Jaccard, D.; et al. *Science* **2007**, *317*, 1196−1199.

(18) Brinkman, A.; Huijben, M.; Van Zalk, M.; Huijben, J.; Zeitler, U.; Maan, J. C.; Van der Wiel, W. G.; Rijnders, G.; Blank, D. H. A.; Hilgenkamp, H. *Nat. Mater.* **2007**, *6*, 493−496.

(19) Lee, P. W.; Singh, V. N.; Guo, G. Y.; Liu, H. J.; Lin, J. C.; Chu, Y. H.; Chen, C. H.; Chu, M. W. *Nat. Commun.* **2016**, *7*, 12773.

(20) Huijben, M.; Brinkman, A.; Koster, G.; Rijnders, G.; Hilgenkamp, H.; Blank, D. H. A. *Adv. Mater.* **2009**, *21*, 1665−1677.

(21) Nakagawa, N.; Hwang, H. Y.; Muller, D. A. *Nat. Mater.* **2006**, *5*, 204−209.

(22) Willmott, P. R.; Pauli, S. A.; Herger, R.; Schleputz, C. M.; Martoccia, D.; Patterson, B. D.; Delley, B.; Clarke, R.; Kumah, D.; Cionca, C.; et al. *Phys. Rev. Lett.* **2007**, *99*, 155502.

(23) Cantoni, C.; Gazquez, J.; Granozio, F. M.; Oxley, M. P.; Varela, M.; Lupini, A. R.; Pennycook, S. J.; Aruta, C.; di Uccio, U. S.; Perna, P.; et al. *Adv. Mater.* **2012**, *24*, 3952−3957.

(24) Salluzzo, M.; Gariglio, S.; Torrelles, X.; Ristic, Z.; Di Capua, R.; Drnec, J.; Sala, M. M.; Ghiringhelli, G.; Felici, R.; Brookes, N. B. *Adv. Mater.* **2013**, *25*, 2333−2338.

(25) Nakamura, M.; Kagawa, F.; Tanigaki, T.; Park, H. S.; Matsuda, T.; Shindo, D.; Tokura, Y.; Kawasaki, M. *Phys. Rev. Lett.* **2016**, *116*, 156801.

(26) Herranz, G.; Basletic, M.; Bibes, M.; Carretero, C.; Tafra, E.; Jacquet, E.; Bouzehouane, K.; Deranlot, C.; Hamzic, A.; Broto, J. M.; et al. *Phys. Rev. Lett.* **2007**, *98*, 216803.

(27) Yin, Y. W.; Burton, J. D.; Kim, Y. M.; Borisevich, A. Y.; Pennycook, S. J.; Yang, S. M.; Noh, T. W.; Gruverman, A.; Li, X. G.; Tsymbal, E. Y.; et al. *Nat. Mater.* **2013**, *12*, 397−402.

(28) Tra, V. T.; Chen, J. W.; Huang, P. C.; Huang, B. C.; Cao, Y.; Yeh, C. H.; Liu, H. J.; Eliseev, E. A.; Morozovska, A. N.; Lin, J. Y.; et al. *Adv. Mater.* **2013**, *25*, 3357−3364.

(29) Spurgeon, S. R.; Sloppy, J. D.; Kepaptsoglou, D. M.; Balachandran, P. V.; Nejati, S.; Karthik, J.; Damodaran, A. R.; Johnson, C. L.; Ambaye, H.; Goyette, R.; et al. *ACS Nano* **2014**, *8*, 894−903.

(30) Anbusathaiah, V.; Kan, D.; Kartawidjaja, F. C.; Mahjoub, R.; Arredondo, M. A.; Wicks, S.; Takeuchi, I.; Wang, J.; Nagarajan, V. *Adv. Mater.* **2009**, *21*, 3497−3502.

(31) Hambe, M.; Petraru, A.; Pertsev, N. A.; Munroe, P.; Nagarajan, V.; Kohlstedt, H. *Adv. Funct. Mater.* **2010**, *20*, 2436−2441.

(32) Sinsheimer, J.; Callori, S. J.; Bein, B.; Benkara, Y.; Daley, J.; Coraor, J.; Su, D.; Stephens, P. W.; Dawber, M. *Phys. Rev. Lett.* **2012**, *109*, 167601.

(33) Kotnala, R. K.; Gupta, R.; Chaudhary, S. *Appl. Phys. Lett.* **2015**, *107*, 082908.

(34) Lorenz, M.; Wagner, G.; Lazenka, V.; Schwinkendorf, P.; Bonholzer, M.; Van Bael, M. J.; Vantomme, A.; Temst, K.; Oeckler, O.; Grundmann, M. *Materials* **2016**, *9*, 44.

(35) Lorenz, M.; Wagner, G.; Lazenka, V.; Schwinkendorf, P.; Modarresi, H.; Van Bael, M. J.; Vantomme, A.; Temst, K.; Oeckler, O.; Grundmann, M. *Appl. Phys. Lett.* **2015**, *106*, 012905.

(36) Gupta, R.; Chaudhary, S.; Kotnala, R. K. *ACS Appl. Mater. Interfaces* **2015**, *7*, 8472−8479.

(37) Sharma, S.; Tomar, M.; Kumar, A.; Puri, N. K.; Gupta, V. *Phys. B* **2014**, *448*, 125−127.

(38) Cazorla, C.; Stengel, M. *Phys. Rev. B: Condens. Matter Mater. Phys.* **2014**, *90*, 020101.

(39) Yang, Y. R.; Stengel, M.; Ren, W.; Yan, X. H.; Bellaiche, L. *Phys. Rev. B: Condens. Matter Mater. Phys.* **2012**, *86*, 144114.

(40) Tang, Y. L.; Zhu, Y. L.; Ma, X. L.; Borisevich, A. Y.; Morozovska, A. N.; Eliseev, E. A.; Wang, W. Y.; Wang, Y. J.; Xu, Y. B.; Zhang, Z. D.; et al. *Science* **2015**, *348*, 547−551.

(41) Nelson, C. T.; Winchester, B.; Zhang, Y.; Kim, S. J.; Melville, A.; Adamo, C.; Folkman, C. M.; Baek, S. H.; Eom, C. B.; Schlom, D. G.; et al. *Nano Lett.* **2011**, *11*, 828−834.

(42) Hartel, P.; Rose, H.; Dinges, C. *Ultramicroscopy* **1996**, *63*, 93−114.

(43) Pennycook, S. J.; Boatner, L. A. *Nature* **1988**, *336*, 565−567.

(44) Tang, Y. L.; Zhu, Y. L.; Wang, Y. J.; Wang, W. Y.; Xu, Y. B.; Ren, W. J.; Zhang, Z. D.; Ma, X. L. *Sci. Rep.* **2015**, *4*, 4115.

(45) Wang, W. Y.; Tang, Y. L.; Zhu, Y. L.; Xu, Y. B.; Liu, Y.; Wang, Y. J.; Jagadeesh, S.; Ma, X. L. *Adv. Mater. Interfaces* **2015**, *2*, 1500024.

(46) Cohen, R. E. *Nature* **1992**, *358*, 136−138.

(47) Jia, C. L.; Mi, S. B.; Urban, K.; Vrejoiu, I.; Alexe, M.; Hesse, D. *Phys. Rev. Lett.* **2009**, *102*, 117601.

(48) Fong, D. D.; Cionca, C.; Yacoby, Y.; Stephenson, G. B.; Eastman, J. A.; Fuoss, P. H.; Streiffer, S. K.; Thompson, C.; Clarke, R.;

DOI: 10.1021/acs.nanolett.7b00788
Nano Lett. 2017, 17, 3619−3628

Pindak, R.; et al. *Phys. Rev. B: Condens. Matter Mater. Phys.* **2005**, *71*, 144112.
(49) Shirane, G.; Hoshino, S. *J. Phys. Soc. Jpn.* **1951**, *6*, 265−270.
(50) Jia, C. L.; Mi, S. B.; Urban, K.; Vrejoiu, I.; Alexe, M.; Hesse, D. *Nat. Mater.* **2008**, *7*, 57−61.
(51) Zhong, W.; Kingsmith, R. D.; Vanderbilt, D. *Phys. Rev. Lett.* **1994**, *72*, 3618−3621.
(52) Torres-Pardo, A.; Gloter, A.; Zubko, P.; Jecklin, N.; Lichtensteiger, C.; Colliex, C.; Triscone, J. M.; Stéphan, O. *Phys. Rev. B: Condens. Matter Mater. Phys.* **2011**, *84*, 220102.
(53) Zhu, G. Z.; Radtke, G.; Botton, G. A. *Nature* **2012**, *490*, 384−387.
(54) Shao, Y.; Hughes, R. A.; Dabkowski, A.; Radtke, G.; Gong, W. H.; Preston, J. S.; Botton, G. A. *Appl. Phys. Lett.* **2008**, *93*, 192114.
(55) Tan, H. Y.; Verbeeck, J.; Abakumov, A.; Van-Tendeloo, G. *Ultramicroscopy* **2012**, *116*, 24−33.
(56) Eerenstein, W.; Morrison, F. D.; Dho, J.; Blamire, M. G.; Scott, J. F.; Mathur, N. D. *Science* **2005**, *307*, 1203−1203.
(57) Wang, X.; Zhu, Y. L.; Mi, S. B.; Wang, C.; Lu, H. B.; Ma, X. L. *Philos. Mag.* **2010**, *90*, 4551−4567.
(58) Moulder, J. F.; Stickle, W. F.; Sobol, P. E.; Bomben, K. D. *Handbook of X-Ray Photoelectron Spectroscopy*; Physical Electronics, Inc., 1992; pp 80−81.
(59) Kim, Y. M.; Morozovska, A.; Eliseev, E.; Oxley, M. P.; Mishra, R.; Selbach, S. M.; Grande, T.; Pantelides, S. T.; Kalinin, S. V.; Borisevich, A. Y. *Nat. Mater.* **2014**, *13*, 1019−1025.
(60) Kim, Y. M.; He, J.; Biegalski, M. D.; Ambaye, H.; Lauter, V.; Christen, H. M.; Pantelides, S. T.; Pennycook, S. J.; Kalinin, S. V.; Borisevich, A. Y. *Nat. Mater.* **2012**, *11*, 888−894.
(61) Yu, P.; Luo, W.; Yi, D.; Zhang, J. X.; Rossell, M. D.; Yang, C. H.; You, L.; Singh-Bhalla, G.; Yang, S. Y.; He, Q.; et al. *Proc. Natl. Acad. Sci. U. S. A.* **2012**, *109*, 9710−9715.
(62) Fiebig, M. *J. Phys. D: Appl. Phys.* **2005**, *38*, R123−R152.
(63) Bousquet, E.; Dawber, M.; Stucki, N.; Lichtensteiger, C.; Hermet, P.; Gariglio, S.; Triscone, J. M.; Ghosez, P. *Nature* **2008**, *452*, 732−736.

DOI: 10.1021/acs.nanolett.7b00788
Nano Lett. 2017, 17, 3619−3628